Article

Interaction of Carbon Nanotube, Capped Carbon Nanotube, C60 Fullerene, and C70 Fullerene with Virulence Factors of Gram-Negative and Gram-Positive Bacteria: The Potential Application for 3D-Printed Scaffolds

Mehran Alavi [1], Morahem Ashengroph [1,*] and M. R. Mozafari [2]

[1] Department of Biological Science, Faculty of Science, University of Kurdistan, Sanandaj, Kurdistan, Iran; mehranbio83@gmail.com

[2] Australasian Nanoscience and Nanotechnology Initiative (ANNI), 8031 Monash University LPO, Clayton, Victoria 3168, Australia; dr.m.r.mozafari@gmail.com

* Correspondence: Morahem Ashengroph; m.ashengroph@uok.ac.ir

Abstract: Antimicrobial application of carbon nanomaterials such as carbon nanotubes (CNTs), capped CNT, C60 fullerene, and C70 fullerene are increasing owing to their low cytotoxicity properties compared to other nanomaterials such as metallic nanoparticles. Enhanced mechanical property and antibacterial activity can be caused by incorporation of CNTs in 3-dimentional (3D) printed nanocomposites (NCs). Interruption of bacterial membrane resulting from cylindrical shape and high aspect ratio properties has been found as the prominent antibacterial mechanism of CNTs. However, unraveling interaction of CNT, capped CNT, C60 fullerene, and C70 fullerene with virulence factors of the main bacterial pathogenesis has not yet been known. Therefore, in the present study, interactions of CNT, capped CNT, C60, and C70 with the eight virulence factors including protein kinase A and ESX-secreted protein B of Mycobacterium tuberculosis, pseudomonas elastase and exotoxin A of Pseudomonas aeruginosa, alpha-hemolysin and penicillin binding protein 2a of Staphylococcus aureus and shiga toxin 2a and heat-labile enterotoxin of Escherichia coli have been evaluated by molecular docking method of AutoDock Vina. This study disclosed the binding strength followed the sequence CNT > capped CNT > C70 > C60 towards alpha-hemolysin of S. aureus compared to other virulence factors with values of -19.6, -18.8, -13.6, and -12.8 kcal/mol, respectively. The lowest and highest binding affinity were found for CNT against 1TII and 1MWT by binding energy values of 97.4 and -20.1 kcal/mol. The stability of CNT-1MWT complex at the different times has resulted according to the normal mode analysis of elNémo and iMOD servers. Future studies should be focused on improving cellular uptake of CNTs, capped CNTs, C70, and C60 by surface functionalization for active targeting of bacteria.

Keywords: 3D printed scaffolds; carbon nanotube; capped carbon nanotube; protein kinase A; pseudomonas elastase; exotoxin A; alpha-hemolysin; shiga toxin 2a

1. Introduction

Emerging antibiotic resistance in various bacterial strains is great therapy challenge, specifically in the case of health-threatening infections such as septicemia and chronic infectious wounds [1–3]. Therefore, there is urgent need for finding new effective biocompatible antibacterial agents. Nanomaterials (NMs), particularly carbon nanotubes (CNTs) and fullerenes can be regarded suitable NMs to hindering bacterial infections because of their unique physicochemical in nanoscale [4]. Moreover, these NMs have been used to upgrade various safe scaffolds for tissue engineering. Providing biocompatible and biodegradable scaffold for tissue engineering is critical to improve

 doi:10.20944/preprints202306.0068.v1

attachment and migration of cells, delivering and retaining cells and biological macromolecules [5]. In this way, various novel techniques have been presented to formation of scaffolds. Three-dimensional (3D) printing technology based on computer-aided design (CAD) software and computed tomography (CT) is promising technique specifically for personalized therapies [6]. In regenerative medicine, 3D printing techniques may be utilized to fabricate implants and scaffolds including calvarial bone grafts and tracheobronchomalacia [7]. In addition, this technology had significant impact on aerospace and mechanical manufacturing [8]. 3D printing techniques are classified according to printing methods and the types of materials. In a fused deposition modeling (FDM)-type printer as the common 3D printing method, the melted filaments of wide range of biocompatible and biodegradable polymers such as poly(ε-caprolactone) (PCL)/thermoplastic polysaccharide can be extruded directly from nozzle and deposited on the substrate as layer-by-layer of the thin film [9]. Four main steps for 3D printing include digital model design, digital slicing, G-code conversion, and manufacturing of the 3D model [10]. As the main advantage, toxic organic solvents are not needed for dissolving the polymeric filaments for this type of printing. Two major limitations for FDM are low-resolution printing and requirement of the high temperature during the melt-extrusion stage, which can change the physicochemical properties of precursors [11]. Application of NMs such as metal nanoparticles (silver, zinc oxide, and copper oxide) and CNTs concomitant with thermoplastic polymers for 3D-rinting has provided novel physicochemical and therapeutic properties. CNTs are produced from carbon atoms by the cylindrical structure (Single-wall carbon nanotubes (SWCNTs) and multi-wall carbon nanotubes (MWCNTs)) intermediate between flat graphene and fullerene cages. SWCNT can be found as chiral, armchair, and zigzag forms. The main configurations of CNTs involving zigzag ($\theta = 0^{o}$) and armchair ($\theta = 30^{o}$) forms are made according to the geometry of the carbon bonds around the circumference of the tube [12]. Moreover, the end of CNTs can be enclosed by fullerene-like cages as capped CNTs [13]. Tough hydrogel incorporated with carbon nanotubes as biohybrid scaffolds accelerated the regeneration of calvarial defect healing in bone regeneration [14]. Additionally, sodium alginate, gelatin, and CNTs were applied to construct cylindrical scaffolds with improved the mechanical properties and low cytotoxicity [15]. In the case of antimicrobial nanocomposites of polylactic acid (PLA) polymer matrix enriched with MWCNT, growth hindering of Escherichia coli and Staphylococcus aureus was observed with higher the mechanical properties [16]. Moreover, SWNTs illustrated significant membrane damage and loss of viability against E. coli after 60 min incubation. The main antibacterial mechanisms for CNTs can be resulted from their cylindrical shape and high aspect ratio followed by their penetration into cell membranes [17]. In the case of fullerenes such as C60 and C70, the main antibacterial mechanisms can be reactive oxygen species (ROS) production specifically $^{1}O_{2}$, DNA damage, cell membrane disruption, and protein denaturation [18]. As a critical point, interaction of CNT, capped CNT, C60, and C70 with biological macromolecules and virulence factors of Gram-negative and Gram-positive bacteria has not yet recognized comprehensively. Direct cytopathic effects, hindering protein synthesis, and interfering with cellular immune functions can be caused by Exotoxin A as the most toxic virulence factor of P. aeruginosa [19]. Tissue damage during infection in the human cells has been founded for Pseudomonas elastase as a major virulence factor of P. aeruginosa [20]. In the case of S. aureus, Alpha-hemolysin as a pore-forming toxin can disrupt the host cell plasma membrane [21]. Penicillin binding protein 2a of methicillin-resistant S. aureus (MRSA) leads to resistance of these bacteria to various antibiotics [22]. M. tuberculosis mediates cell growth and survival in vitro and in vivo by Protein kinase A (PknA) [23]. In addition, mycobacterial ESX-secreted protein B contributes to the survival of M. tuberculosis against the immune system via suppressing interferon-γ-induced autophagy in macrophages and damaging the phagosome membrane [24]. For E. coli, heat-labile enterotoxin causes watery diarrhea in enterotoxigenic E. coli infection and Shiga toxin related to E. coli O157:H7 leads to bloody diarrhea hemolytic uremic syndrome [25,26]. In this way, we have tried to reveal interaction of carbon nanotube and capped carbon nanotube with the main virulence factors including Escherichia coli (heat-labile enterotoxin and shiga toxin), Mycobacterium tuberculosis (ESX-secreted protein B and the serine/threonine

Preprints (www.preprints.org) | NOT PEER-REVIEWED | Posted: 5 June 2023 doi:10.20944/preprints202306.0068.v1

protein kinase), P. aeruginosa (pseudomonas elastase and exotoxin A), and Staphylococcus aureus (alpha-hemolysin and protein 2a) by molecular docking.

In this way, we have tried to reveal interaction of carbon nanotube and capped carbon nanotube with the main virulence factors including protein kinase A of Mycobacterium tuberculosis, pseudomonas elastase and exotoxin A of Pseudomonas aeruginosa, alpha-hemolysin of S. aureus, and shiga toxin 2a of E. coli by molecular docking.

2. Materials and Methods

2.1. Molecular docking preparation

Five virulence factors of E. coli; shiga toxin 2a (ID: 7D6Q and resolution: 1.80 Å) and heat-labile enterotoxin (ID: 1TII and resolution: 2.25 Å), S. aureus; alpha-hemolysin (ID: 7AHL and resolution: 1.89 Å) and penicillin-binding protein 2a (ID: 1MWT and resolution: 2.45 Å), M. tuberculosis; protein kinase A (ID: 4OW8 and Resolution: 2.03 Å) and mycobacterial ESX-secreted protein B (ID: 7P13 and resolution: 2.29 Å), and P. aeruginosa; elastase (ID: 1EZM and resolution: 1.50 Å) and exotoxin A (1IKQ and resolution: 1.62 Å) (Figure 1a–h) were obtained from Research Collaboratory for Structural Bioinformatics (RCSB) as the receptors (http://www.rcsb.org/). Grid box parameters (7D6Q; center_x =2.95, center_y =33.76, center_z =0.39, size_x = 68, size_y = 94, and size_z = 62 Å), (7AHL; center_x = 49.29, center_y = 32.77, center_z = 42.17, size_x = 92, size_y = 76, and size_z = 92 Å), (4OW8; center_x = -2.54, center_y = 6.46, center_z = -18.05, size_x = 54, size_y = 40, and size_z = 44 Å), (1EZM; center_x = 45.75, center_y = 33.09, center_z = 28.00, size_x = 40, size_y = 58, and size_z = 46 Å), and (1IKQ; center_x = 32.10, center_y = 36.45, center_z = 16.80, size_x = 78, size_y = 56, and size_z = 60 Å) were determined by AutoDock Vina 1.1.2 based on blind cocking [27]. Armchair CNT (5,5) and capped CNTs ligands with a diameter of ~1 nm and length of ~2 as well as C60 and C70 by a diameter of ~1 nm were prepared by material studio 2017 for evaluation of a ligand-receptor interaction (Figure 2a–d) [28]. UCSF Chimera1.12 program was used to prepare the optimized structures of ligands followed by removing all the water molecules. Molecular dockings of a ligand-receptor and visualization of results were carried out by the ADV1.1.2 and Discovery Studio Visualizer (DSV) 2016 [29].

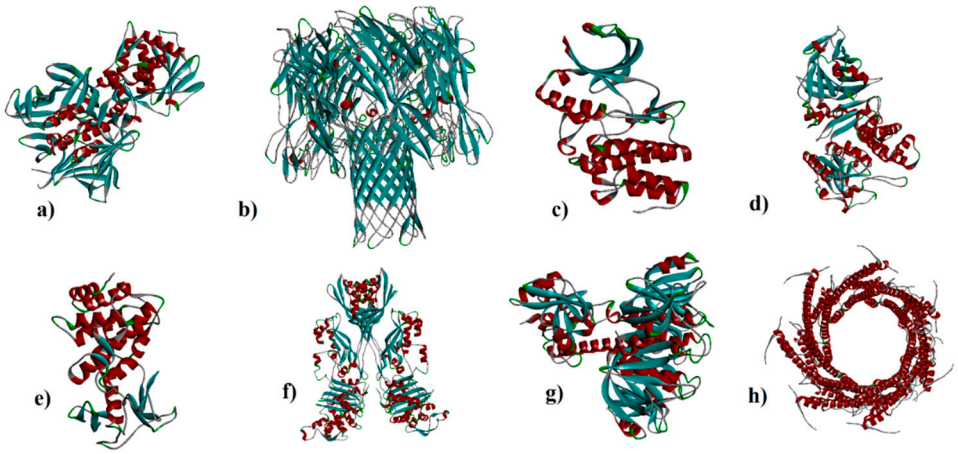

Figure 1. a) 7D6Q, b) 7AHL, c) 4OW8, d) 1IKQ, e) 1EZM, f) 1MWT, g) 1TII, and h) 7P13.

Preprints (www.preprints.org) | NOT PEER-REVIEWED | Posted: 5 June 2023 doi:10.20944/preprints202306.0068.v1

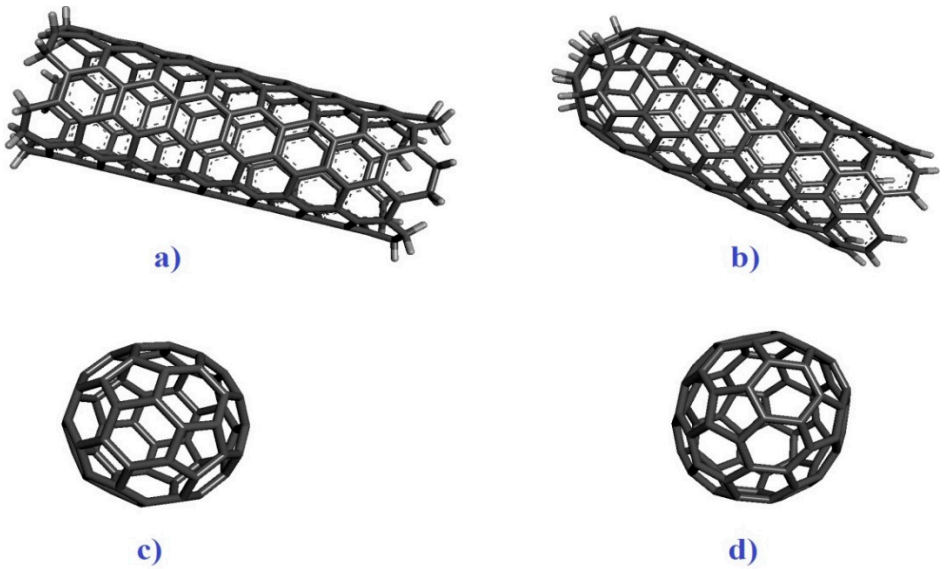

Figure 2. a) armchair CNT (5,5), b) capped CNT, c) C60, and d) C70.

2.2. The normal mode analysis

Each normal mode for the collective functional motions of biological macromolecules comprises a frequency and a deformation, which can be evaluated by iMOD server. iMOD can provide simulation or the normal mode analysis of trajectories between two conformations and interactively. Since the molecular docking may not be fully reliable, molecular dynamic simulation of the prominent docking interaction was selected to obtain the normal mode analysis study [30]. The structural dynamics and molecular motion of the docking complex were evaluated via iMOD server [31]. Co-variance map, complex deformability, elastic network, B-factor, and eigenvalues, variance can be indicated by this web server [32]. The results were presented keeping all the parameters as default [33]. Additionally, the elastic network model of elNémo server was used to evaluate the contribution of each normal mode to its conformational change for a main docked interaction by the highest binding energy [34].

3. Results

3.1. Molecular docking

In this study, interaction of the carbonic NMs including CNT, capped CNT, C60, and C70 with the major virulence factors of shiga toxin 2a (Figure 3), alpha-hemolysin (Figure 4), protein kinase A (Figure 5), elastase (Figure 6) exotoxin A (Figures 7), heat-labile enterotoxin (Figure 8), penicillin-binding protein 2a (Figure 9), and ESX-secreted protein B (Figure 10). Generally, docking scores obtained from AutoDock Vina disclosed that CNTs compared to fullerenes had more affinity for bacterial virulence factors (Tables 1 and 2). This may be resulted from morphology of CNTs with their tubular shape compared with spherical shape of fullerene. In the case of CNT, lower and higher energies of affinity with values of -19.6 and -11.9 kcal/mol were found for 7AHL and 1EZM receptors, respectively (Table 1). For CNT and 7AHL receptor, there were interacting amino acids including THR125, LYS131, LEU135, ASN121, ASN123, LEU135, ASN121, ASN123, LEU135, ASN121, THR125, GLY126, and ASP127. Among the all receptors, the lowest and highest binding affinity were found for CNT against 1TII and 1MWT by binding energy values of 97.4 and -20.1 kcal/mol (Table 1). Common interacting amino acids for CNT-1MWT and capped CNT-1MWT complexes were ASN146, LYS148, GLU170, GLN199, GLN200, GLN203, TRP205, PRO213, THR238, PRO258, ILE259, ASP274, ASP275, and ILE309 (Figure 9). Based on different interacting amino acids for these ligands, asparagine (ASN236 and ASN260: aliphatic amino acid) and serine (SER261: a polar amino acid) have found specifically for CNT-1MWT docking complex (Table 1and Figure 9). Moreover, donor/acceptor

Preprints (www.preprints.org) | NOT PEER-REVIEWED | Posted: 5 June 2023 doi:10.20944/preprints202306.0068.v1

surface for best pose in terms of H-bond interaction of CNT-1MWT was indicated in solid surface by X, Y, and Z sizes of 5.67, 24.63, and -22.64 Å, respectively (Figure 11).

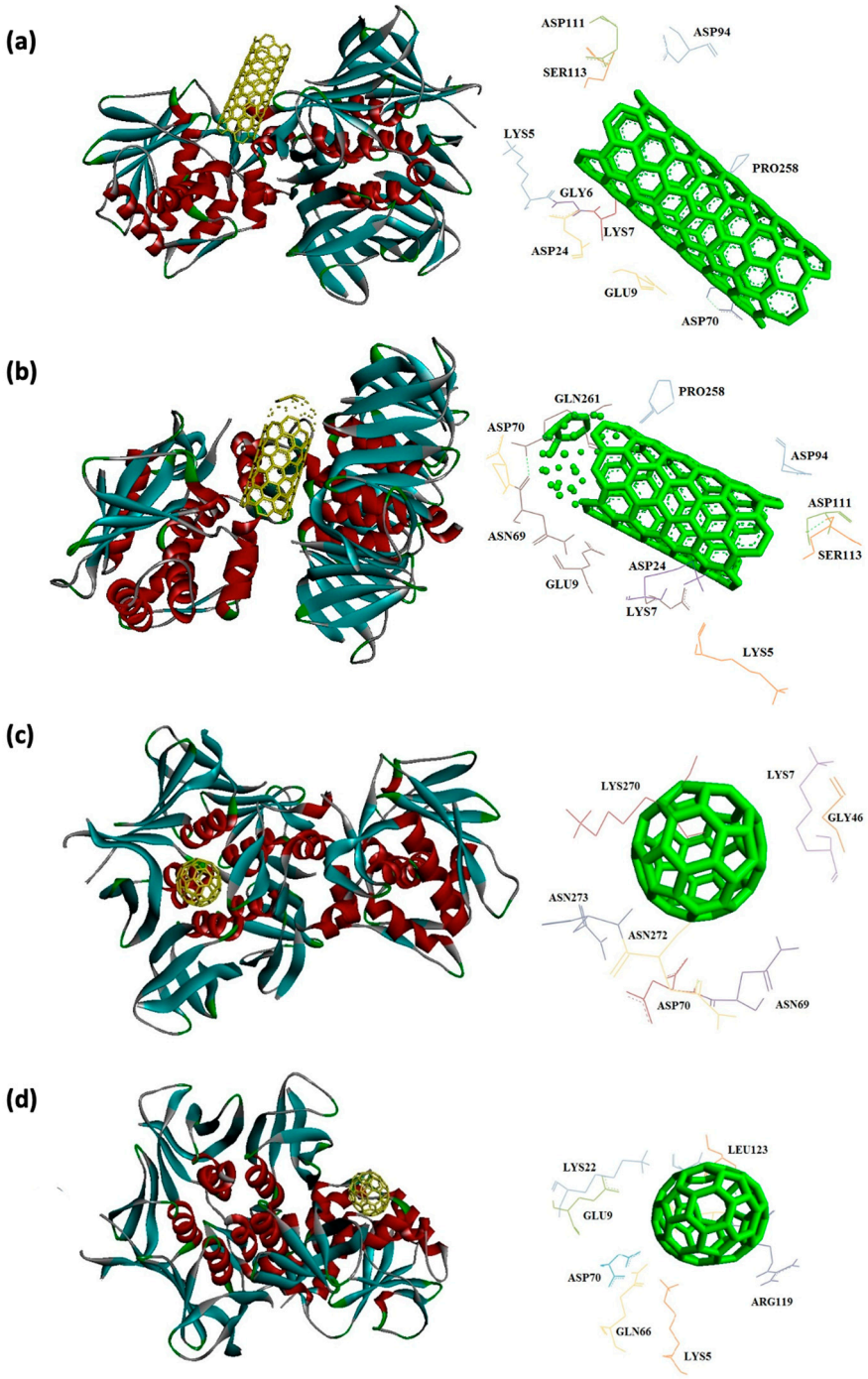

Figure 3. Interaction of 7D6Q with CNT (a), capped CNT (b), C60 (c) and C70 (d).

Preprints (www.preprints.org) | NOT PEER-REVIEWED | Posted: 5 June 2023 doi:10.20944/preprints202306.0068.v1

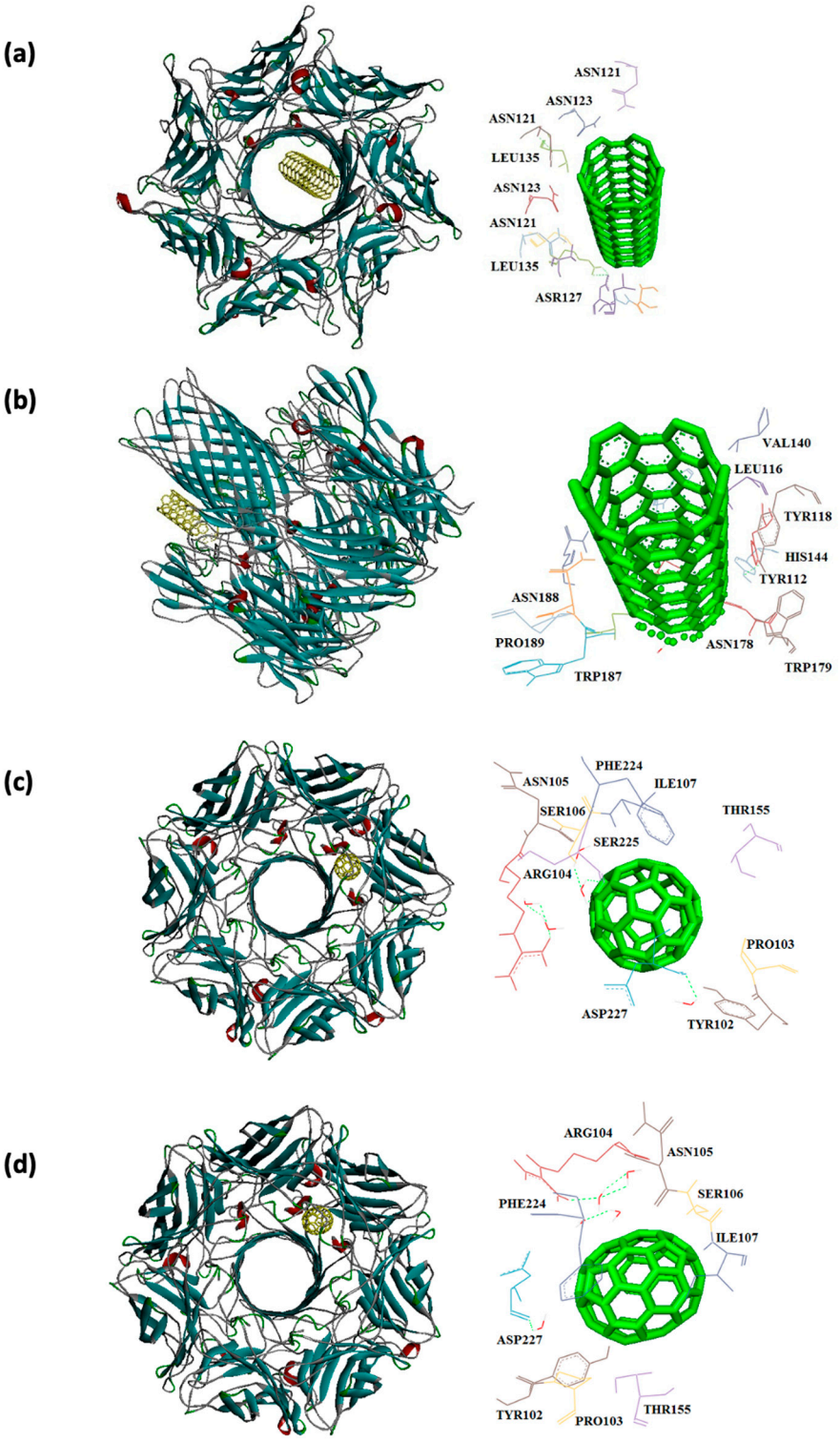

Figure 4. Interaction of 7AHL with CNT (a), capped CNT (b), C60 (c) and C70 (d).

 doi:10.20944/preprints202306.0068.v1

Table 1. Binding affinities (kcal/mol) and interacting residues contributing to interaction of CNT and capped CNT with 7D6Q, 7AHL, 4OW8, 1IKQ, and 1EZM receptors.

Receptors	Binding affinity for CNT	Interacting amino acids	Binding affinity for capped CNT	Interacting amino acids
7D6Q	-14.4	ASP94, ASP111, SER113, PRO258, ASP70, LYS5, GLY6, LYS7, GLU9, and ASP24	-16.1	ASP94, ASP111, SER113, PRO258, GLN261, ASN69, ASP70, LYS5, LYS7, GLU9, and ASP24
1TII	97.4	GLU22, THR24, LYS25, SER42, SER74, GLY75, MET76, ARG77, GLY1, ALA98, ARG15, ARG16, GLY18, ALA28, TYR29, GLU30, ARG31, LEU119, ARG141, ASP142	79	GLU22, THR24, LYS25, SER42, SER74, GLY75, MET76, ARG77, GLY1 ALA98, ARG15 ARG16, GLY18 ALA28, GLU30 ARG31, LEU119 ARG141, ASP142
7AHL	-19.6	THR125, LYS131, LEU135, ASN121, ASN123, LEU135, ASN121, ASN123, LEU135, ASN121, THR125, GLY126, and ASP127	-18.8	LEU116, TYR118, VAL140, TYR112, HIS144, TRP179, PRO181, TYR182, SER186, TRP187, ASN188, PRO189, GLN194, ASN178, and TRP179
1MWT	-20.1	ASN146, LYS148, GLU170, GLN199, GLN200, GLN203, TRP205, PRO213, ASN236, THR238, PRO258, ILE259, ASN260, SER261, ASP274, ASP275, ILE309	-19.6	ASN146, LYS148, GLU170, GLN199, GLN200 GLN203, TRP205 PRO213, THR238, PRO258 ILE259, ASP274, ASP275 ARG298, ILE309
4OW8	-13.0	ARG112, SER212, LYS214, PRO216, ALA218, LYS228,	-12.6	ARG112, SER212, LYS214, PRO216, ALA218, LYS228, PRO235, PRO238,

 doi:10.20944/preprints202306.0068.v1

		PRO235, PRO238, and ASP240		and ASP240
7P13	-16.6	ALA186, ASP189 GLN190, ASN274 GLN190, GLN193 HIS197, PRO276 LYS277, PRO279 PRO280	-16.3	ALA186, ASP189 GLN190, GLN190 GLN193, HIS197 PRO276, LYS277 PRO279, PRO280
1IKQ	-12.9	ARG213, ASN215, ASP218, GLU221, ASP403, and GLU431	-13.2	ARG213, ASN215, ASP218, GLU221, and GLU431
1EZM	-11.9	ASN112, TYR114, TRP115, ASP116, ASP136, GLU148, TYR155, GLU172, GLU175, ASP183, and LEU185	-12.3	ASN112, TRP115, ASP116, ASP136, GLU148, TYR155, GLU172, GLU175, ASP183, and LEU185

Capped CNT showed -18.8 and -12.3 kcal/mol of binding energies for these virulence factors, respectively. In the case of 7AHL and capped CNT, residues of LEU116, TYR118, VAL140, TYR112, HIS144, TRP179, PRO181, TYR182, SER186, TRP187, ASN188, PRO189, GLN194, ASN178, and TRP179 were interacted in binding site (Figure 4b). There was no significant difference between C60 and C70 towards all receptors (Table 2). More affinity values of -12.8 and -13.6 kcal/mol were observed for C60 and C70 against 7AHL, respectively. Interacting amino acids of ARG104, ASN105, SER106, ILE107, TYR102, PRO103, THR155, PHE224, SER225, and ASP227 were contributed to interaction of C70 with 7AHL. Interaction of C60 with 7AHL showed ARG104, ASN105, SER106, ILE107, TYR102, PRO103, THR155, PHE224, SER225, and ASP227 interacting amino acids. Additionally, C60 and C70 had lower binding affinities less than -8 kcal/mol toward 1IKQ and 1EZM virulence factors. Therefore, results illustrated higher affinity of CNT, capped CNT, C70, and C60 toward alpha-hemolysin (7AHL) of S. aureus compared with other receptors by values of -19.6, -18.8, -13.6, and -12.8 kcal/mol.

 doi:10.20944/preprints202306.0068.v1

Table 2. Binding affinities (kcal/mol) and interacting residues contributing to interaction of C60 and C70 with 7D6Q, 7AHL, 4OW8, 1IKQ, and 1EZM receptors.

Receptors	Binding affinity for C60	Interacting amino acids	Binding affinity for C70	Interacting amino acids
7D6Q	-10.1	LYS270, ASN272, ASN273, LYS7, GLY46, ASN69, ASP70	-10.0	GLN118, ARG119, LEU123, GLU124, LYS5, GLN66, ASP70, GLU9, LYS22
1TII	-4.9	THR24, LYS25, SER42, GLY1, ALA98, ARG141	-2.5	GLU22, THR24, LYS25, SER42, GLY1, ALA98 ARG15, ARG141, ASP142
7AHL	-12.8	ARG104, ASN105, SER106, ILE107, TYR102, PRO103, THR155, PHE224, SER225, ASP227	-13.6	ARG104, ASN105, SER106, ILE107, TYR102, PRO103, THR155, PHE224, SER225, ASP227
1MWT	-10.4	TYR255, ASN260 PHE371, GLY374 MET375, ASN377 TYR380	-11.4	TYR255, ASN260 LYS280, PHE371 GLY374, MET375 ASN377, TYR380
4OW8	-8.3	LEU190, HIS192, ILE230, LYS255, ASN256	-8.1	LEU190, HIS192, ILE230, LYS255, ASN256
7P13	-9.7	THR262, GLU263 ASN266, TYR211 GLN214, TRP218	-10.5	LYS259, THR262 GLU263, ASN266 TYR211, GLN214 LEU215, TRP218 GLU263, LYS267
1IKQ	-7.5	HIS107, ASP139, ARG276, ARG279	-7.6	ASN215, GLU221, ASP403, GLN428
1EZM	-7.6	TRP115, ASP116, GLY117, TYR155	-7.7	TRP115, ASP116, GLY117, TYR155

Preprints (www.preprints.org) | NOT PEER-REVIEWED | Posted: 5 June 2023 doi:10.20944/preprints202306.0068.v1

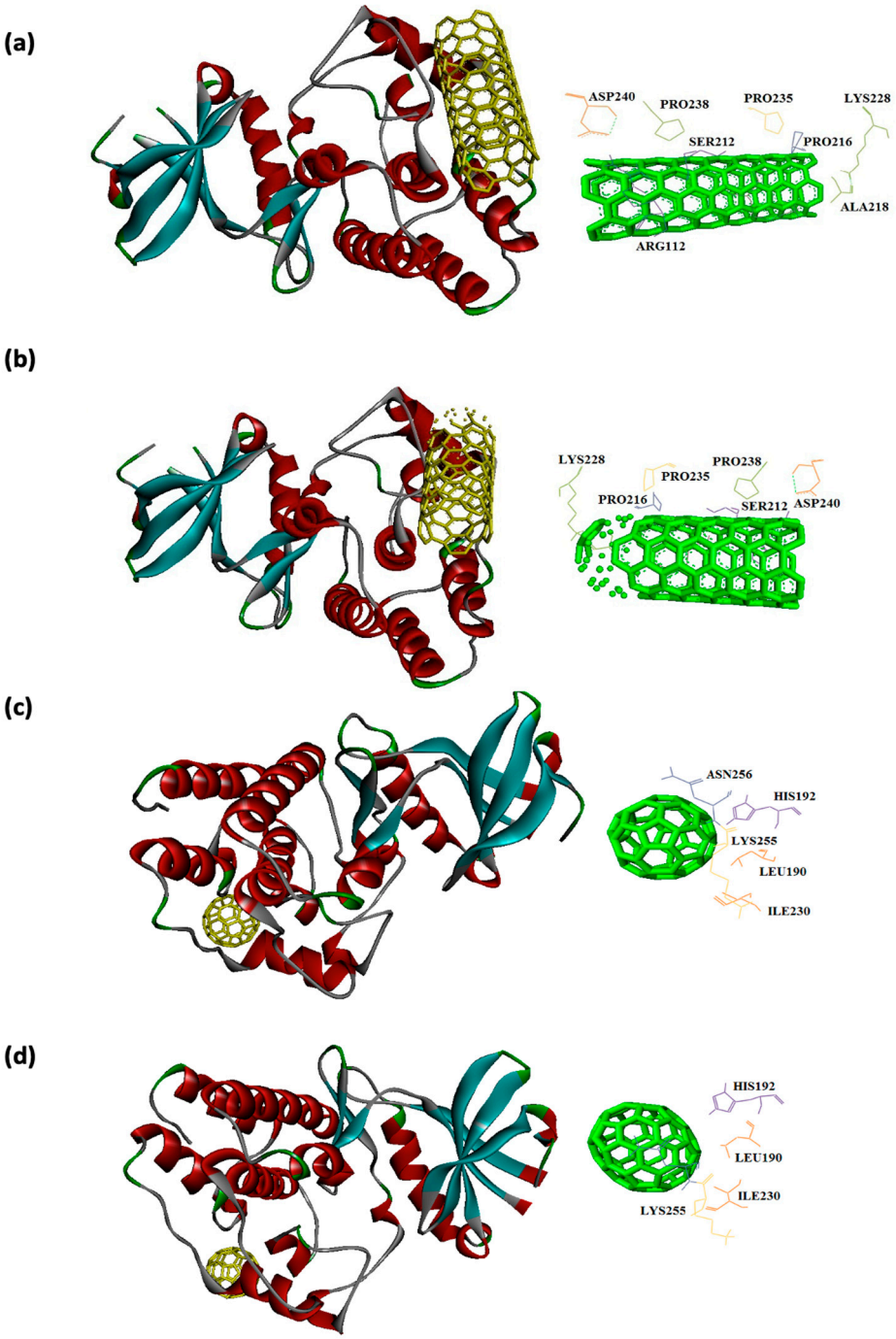

Figure 5. Interaction of 4OW8 with CNT (a), capped CNT (b), C60 (c) and C70 (d).

Preprints (www.preprints.org) | NOT PEER-REVIEWED | Posted: 5 June 2023 doi:10.20944/preprints202306.0068.v1

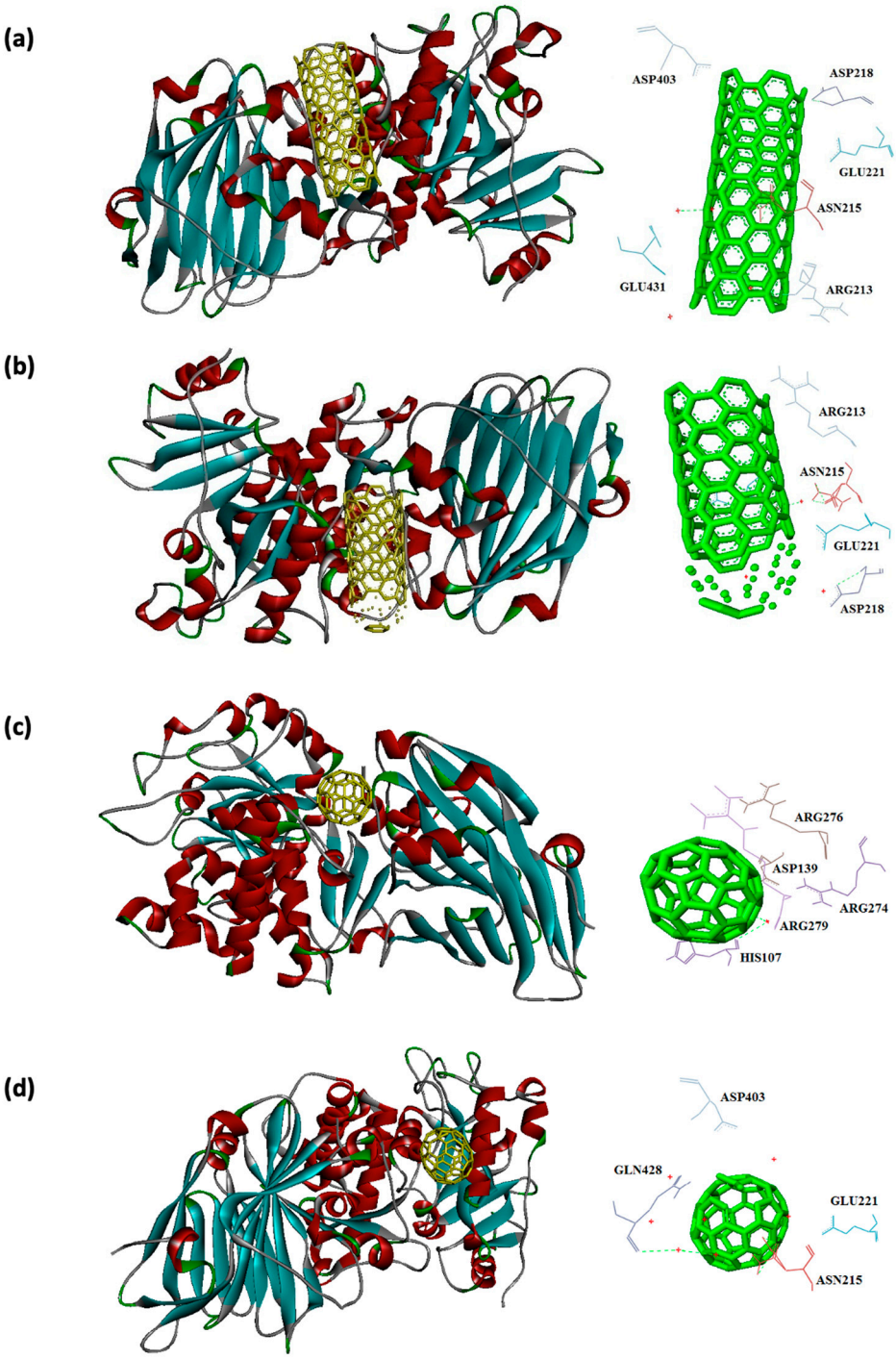

Figure 6. Interaction of 11KQ with CNT (a), capped CNT (b), C60 (c) and C70 (d).

Preprints (www.preprints.org) | NOT PEER-REVIEWED | Posted: 5 June 2023 doi:10.20944/preprints202306.0068.v1

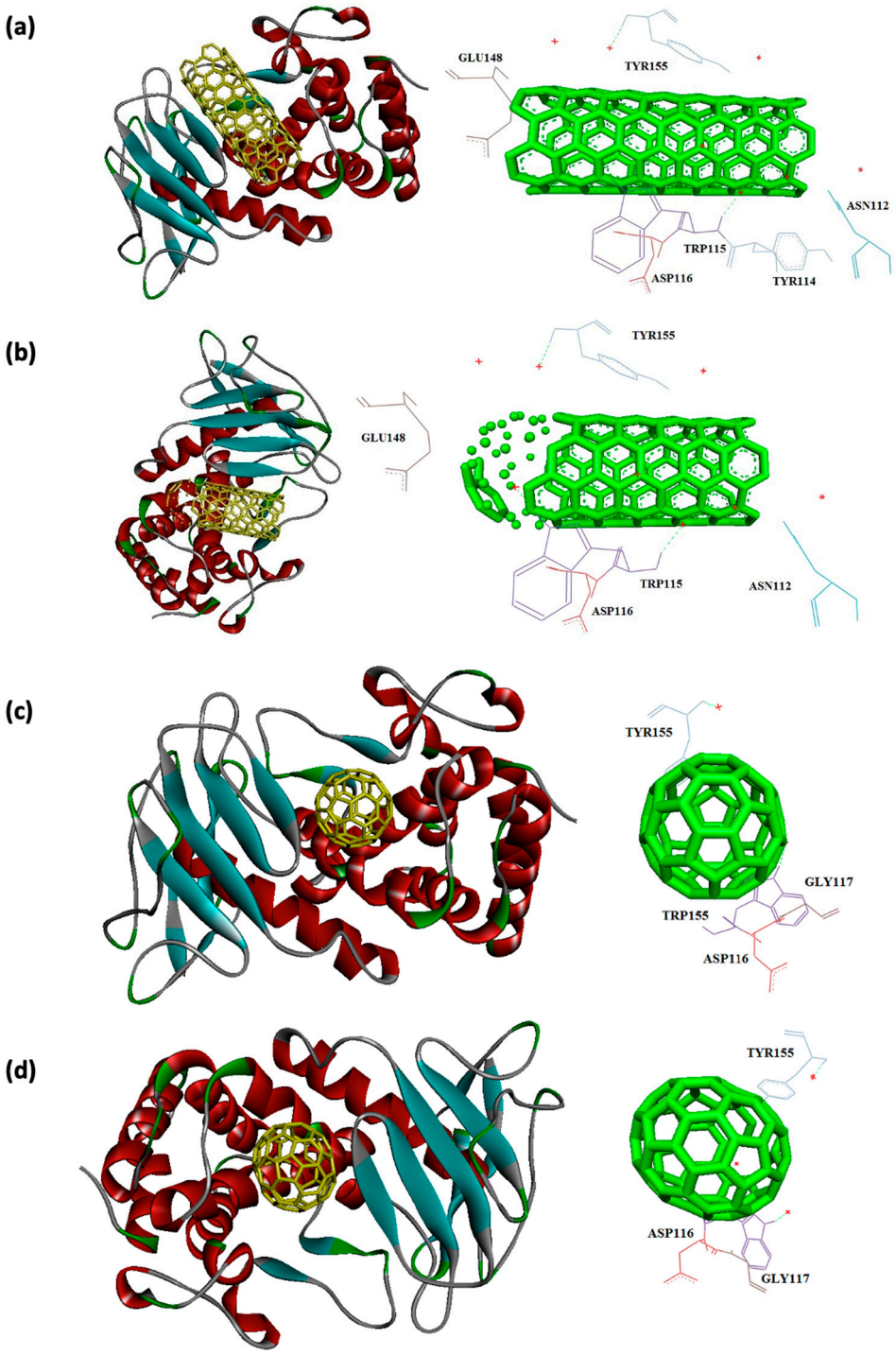

Figure 7. Interaction of 1EZM with CNT (a), capped CNT (b), C60 (c) and C70 (d).

Preprints (www.preprints.org) | NOT PEER-REVIEWED | Posted: 5 June 2023 doi:10.20944/preprints202306.0068.v1

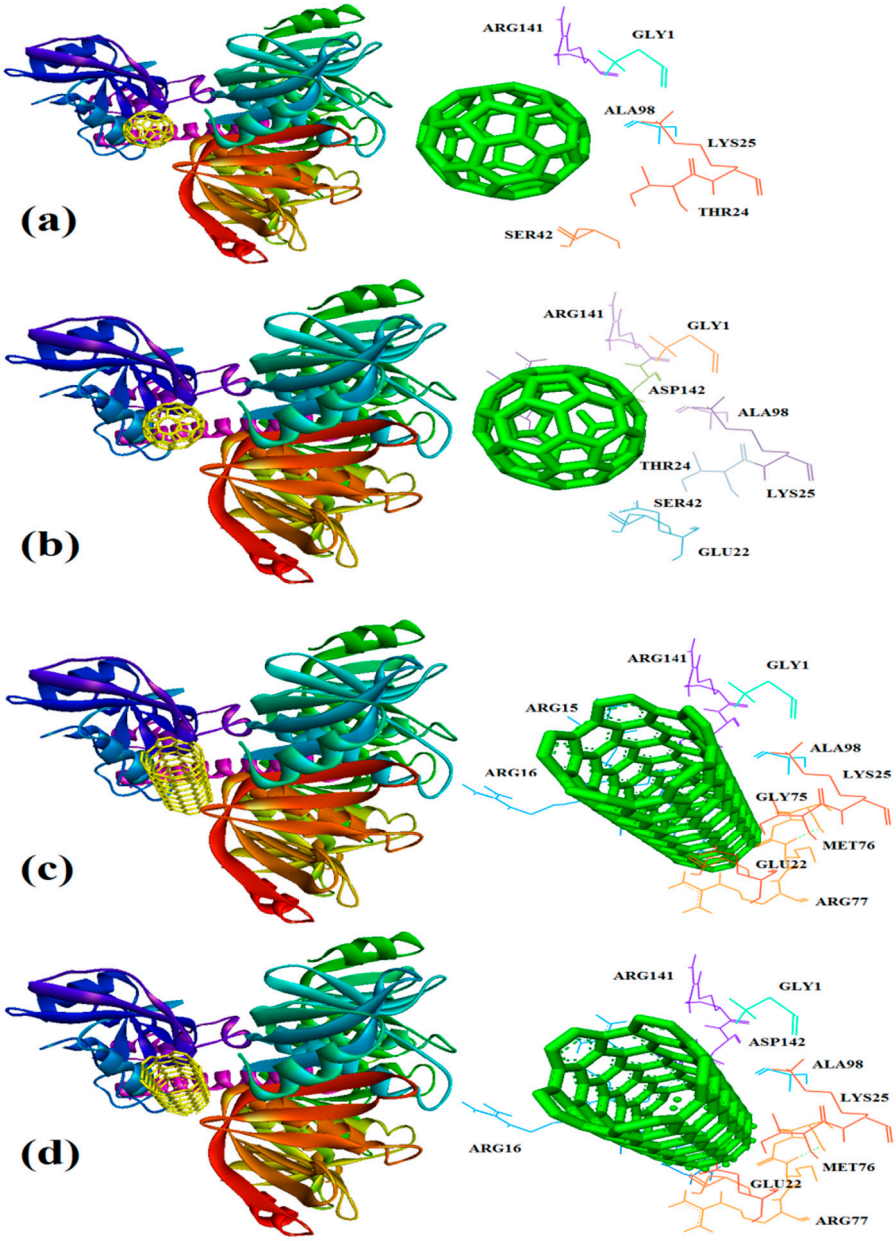

Figure 8. Interaction of 1TII with C60 (a) and C70 (b) CNT (c), capped CNT (d).

Preprints (www.preprints.org) | NOT PEER-REVIEWED | Posted: 5 June 2023 doi:10.20944/preprints202306.0068.v1

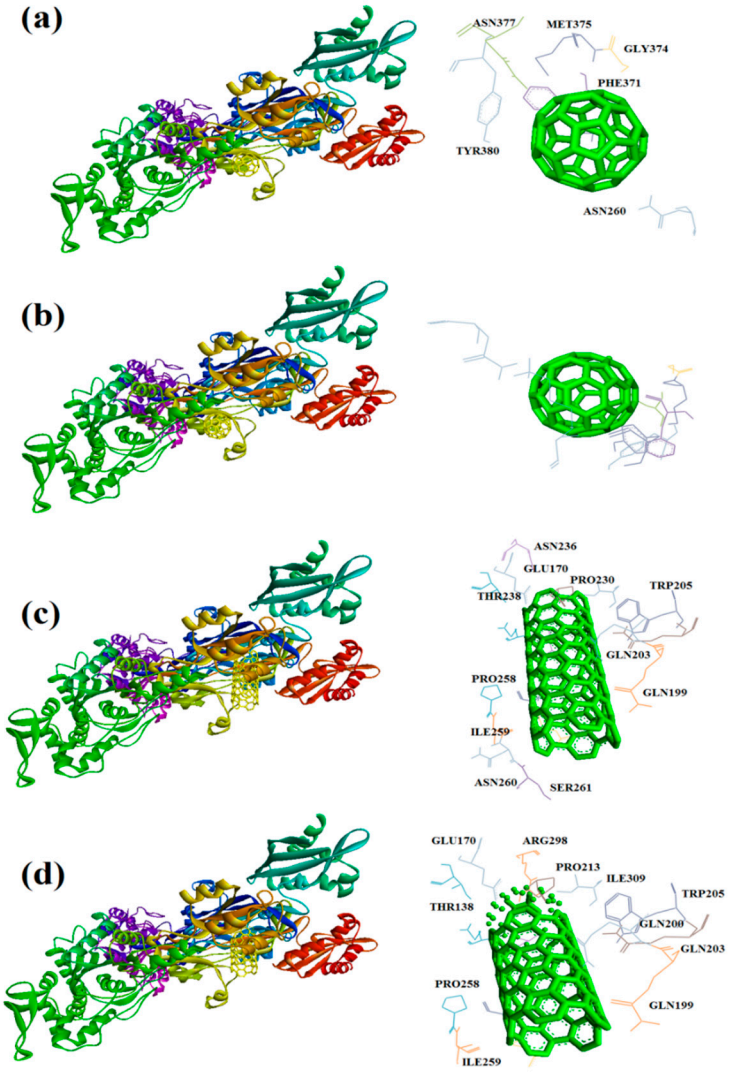

Figure 9. Interaction of 1MWT with C60 (a) and C70 (b) CNT (c), capped CNT (d).

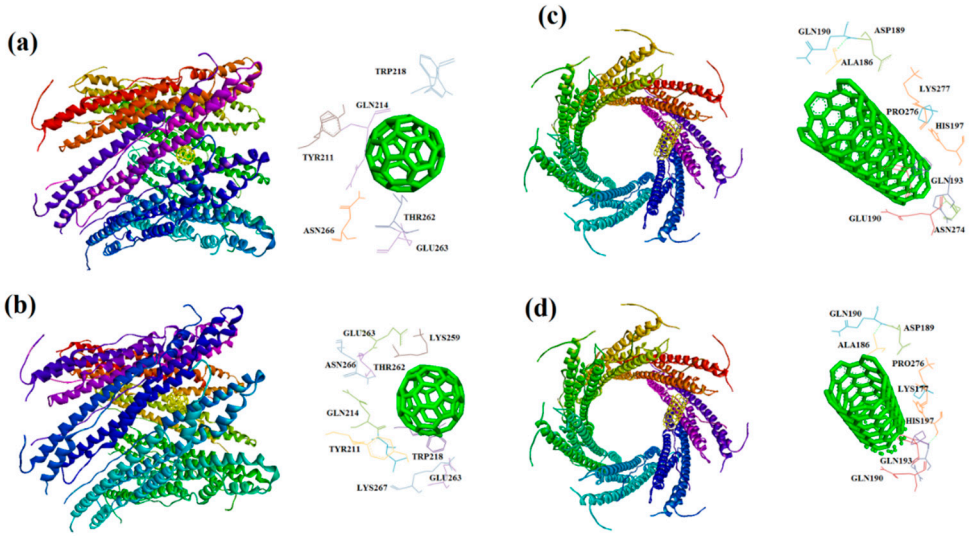

Figure 10. Interaction of 7P13 with C60 (a) and C70 (b) CNT (c), capped CNT (d).

Preprints (www.preprints.org) | NOT PEER-REVIEWED | Posted: 5 June 2023 doi:10.20944/preprints202306.0068.v1

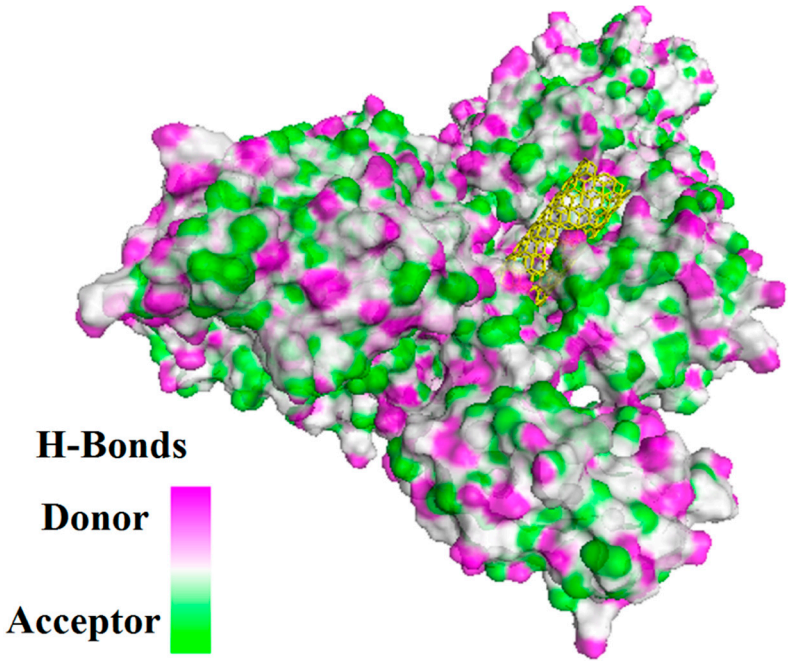

Figure 11. Solvent hydrogen bond donor/acceptor surface for CNT-1MWT was indicated in solid surface by X, Y, and Z sizes of 5.67, 24.63, and -22.64 Å, respectively.

3.2. The normal mode analysis

Frequency and deformation parameters were obtained by each normal mode analysis. In the case of deformation, simulation or the normal mode analysis of trajectories are critical to evaluating changes between two conformations. Moreover, the collective functional motions of biological macromolecules can be measured by normal mode analysis in IMOD server [30]. The docking complex of CNT-1MWT with the highest binding affinity was employed for the normal mode analysis study and molecular simulation using iMOD and elNémo servers. Molecular mobility (Figure 12a), the main-chain deformability (Figure 12b) and B-factor (Figure 12c) have been obtained for the complex of CNT-1MWT. There were the locations with deformability the regions of 1MWT protein (Figure 12b). Stable structure for CNT-1MWT complex was predicted by the B-factor analysis (Figure 12c) based on the mean of the root mean square (RMS). A variance plot (Figure 13a), eigenvalue (Figure 13b), covariance map (Figure 13c), and elastic network model (Figure 13d) were obtained for the normal modes. The easier deformation of the macromolecule can be predicted by a lower value of the eigenvalue. The eigenvalue for each normal mode showed the motion stiffness by a value of 1.379e-05 (Figure 13b). Red, white, and blue colors exhibit correlated, uncorrelated, and anti-correlated motions, respectively based on the covariance matrix analysis (Figure 13c). Additionally, rigidity and flexibility of springs between (Cα) atoms of docked protein molecule have been indicated as the darker and brighter colors (Figure 13d) [35]. For clarifying conformational change of CNT-1MWT complex, a snapshot at 0ns, 11ns, 22 ns, 33 ns, and 44 ns are illustrated in Figure 14a [36]. The root mean square deviation (RMSD) of ligand atoms can show a stability level of docked complex (Figure 14b) [37]. CNT exhibited the stability within the active site at equilibrium at 1.4 Å of RMSD at around 11 ns.

Preprints (www.preprints.org) | NOT PEER-REVIEWED | Posted: 5 June 2023 doi:10.20944/preprints202306.0068.v1

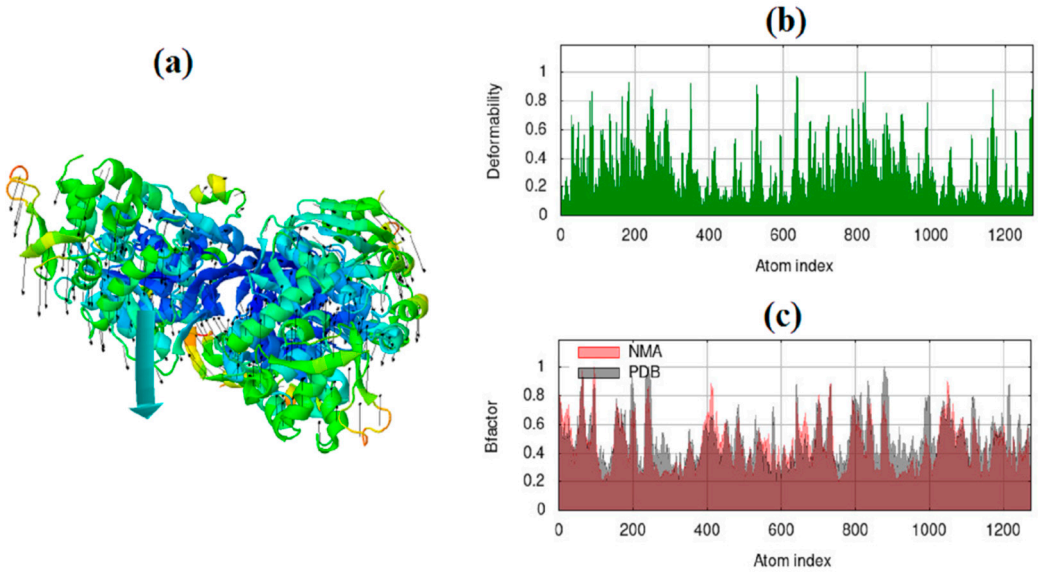

Figure 12. Molecular mobility (a) (Two colored affine-arrows showing the domains mobility) the main-chain deformability (b) and B-factor evaluated by NMA of the main docked complex of 1MWT -CNT.

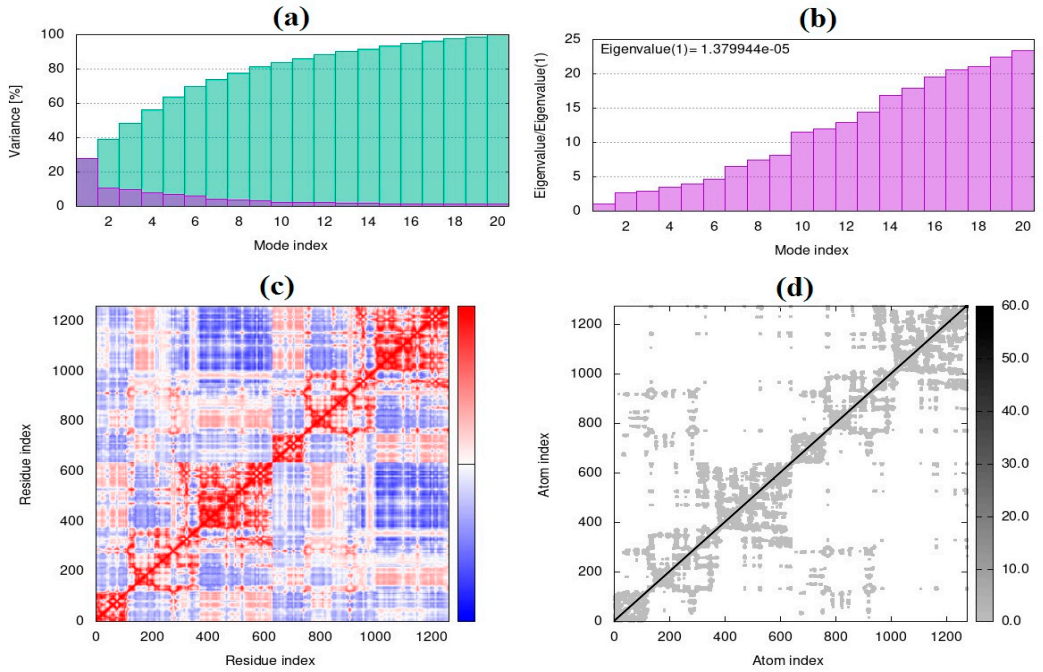

Figure 13. Results of iMODS for variance plot (a) (Colored bars show the cumulative (green) and individual (red) variances), eigenvalue (b), covariance matrix analysis (c), and elastic network model (d) for 1MWT -CNT.

Preprints (www.preprints.org) | NOT PEER-REVIEWED | Posted: 5 June 2023 doi:10.20944/preprints202306.0068.v1

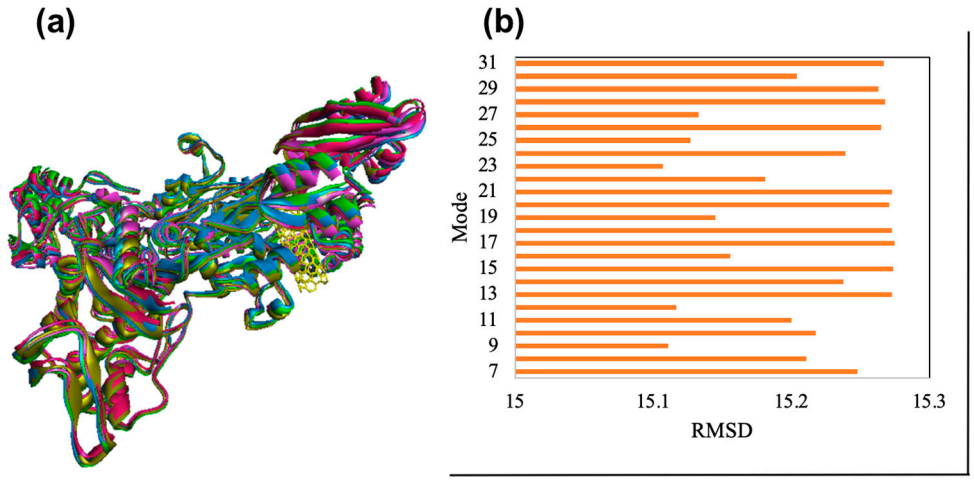

Figure 14. The aligned structures of CNT (yellow color)-1MWT during simulation; green 0ns, blue 11ns, olive 22 ns, violet 33 ns, and red 44 ns (a). RMSD of the docked complex at the different modes based on the results of elNémo server (b).

4. Discussion

Bacterial pathogeneses by various virulence factors as secretory, membrane associated or cytosolic forms can colonize and damage the host cells [38]. For example, in the case of M. tuberculosis, protein kinase A is critical factor for growth and has been considered as possible drug target [39]. Pseudomonas elastase is a major virulence factor in P. aeruginosa that regulated by the lasR gene and lead to extensive tissue damage [40]. Exotoxin A of P. aeruginosa inhibit protein synthesis and interferes with cellular immune functions [41]. Alpha-hemolysin of S. aureus, a pore forming toxin, can penetrates cell membranes and leading to osmotic swelling and lytic of erythrocytes [42]. Gastrointestinal disease and hemolytic uraemic syndrome can be resulted from shiga toxin 2a of E. coli [43].

In a similar study, docking of fullerene C60 against several receptors of drug resistant Salmonella typhi, was evaluated by AutoDock Vina. This study disclosed that C60 can form stable interaction with receptors of ssrB, slrP, and PhoQ by values of −12.9, −12.8, and −12.2 kcal/mol respectively. For interaction of C60 with ssrB, interacting amino acids were Gly 116, Arg 186, Pro 238, Pro 278, and Pro 281 [44]. Antimicrobial activities of CNTs and fullerene have been reported by several studies [45,46]. Physical membrane damage, production of reactive oxygen species, and disruption of metabolic pathways are the main antibacterial mechanisms of CNT. Antibacterial activity of CNT can be affected by its diameter, length, surface chemistry, and surface functional groups properties. In addition, characteristics of bacteria including type and morphology, mechanical properties of cell wall, and growth state (planktonic and biofilm forms) can determine antibacterial capacity of CNT. In addition, surface modification of CNT by antimicrobial compounds, metal/metal oxide NPs, amino acids, and polymers have shown different antibacterial activities as inhibiting of cell wall, oxidative stress, and promotion of the contact between CNTs or MWCNTs and bacterial cell wall [47]. E. coli and Salmonella typhimurium were inhibited by functionalized MWCNTs by lysine and arginine. Increased antibacterial activity of this nanocomposite was resulted from electrostatic adsorption of bacteria membrane because of positive charges of lysine and arginine on MWCNTs surface [48]. 3D-nanostructures composed of graphene–carbon nanotubes–iron oxides had higher adsorption and antibacterial capacity toward E. coli and S. aureus [49]. Thin film based on polymer shielded Ag nanoparticle loaded oxidized CNT prepared by the spray-assisted layer-by-layer assembly, showed significant antibacterial activity against Gram positive S. aureus and Gram negative E. coli [50]. Antibiotics may be used to surface functionalize CNTs or MWCNTs and synergize their antibacterial

 doi:10.20944/preprints202306.0068.v1

activity. In this way, covalent grafting of antibiotic with surface-modified CNTs was applied to conjugate levofoxacine with MWCNT. In low effective dose, there was higher sensitivity of S. aureus compared to Pseudomona aeruginosa. This may be resulted from different cell wall morphology of Gram-negative and Gram-positive [51]. In infected chronic wounds and septicemia, hindering and eradication of bacterial growth in physiological conditions is the critical issue [52,53]. In this aspect, for increasing cellular uptake of CNTs and capped CNTs, other surface functionalization strategies including shortened CNT bifunctionalized with amphotericin B, CNT bifunctionalized with ammonium groups, ammonium-functionalized CNT, CNT functionalized with fluorescein isothiocyanate and acetamidofunctionalized CNT, CNT bifunctionalized with methotrexate can be regarded to future investigations [54]. The major limitation for antibacterial efficiency of fullerene is its hydrophobicity, which can be improved by surface functionalization including esterification (fullerene –COOR), carboxylation (fullerene–COOH), and hydroxylation (fullerene–OH). Increased hydrophilic property augmented the contact between lysozyme and fullerene, which followed by more conformational changes and significant antibacterial effect [55]. Moreover, other derivatives of C60 fullerene such as fulleropyrrolidine C60, and dicationic fulleropyrrolidinium, have exhibited supreme bactericidal activity against Gram-negative and Gram-positive bacteria [18]. Functionalization of fullerenol (polyhydroxylated fullerene) by antibacterial drug, sulfasalazine caused increased antibacterial activity against both Gram-negative and Gram-positive bacteria [56]. Application of carbon nanomaterials such as graphenes, fullerenes, and CNTs in 3D printed scaffolds is increasing because their biocompatibility, therapeutic, electrical, mechanical, and thermomechanical properties. Electrical stimulation can impact on human cell viability and bacterial growth of Gram-negative and Gram-positive bacteria. In this regard, 3D printed electroactive scaffolds composed of polycaprolactone and conductive thermally reduced graphene oxide (TrGO) nanoparticles showed significant antibacterial activity against S. aureus on the surface of scaffolds [57]. In the case of MWCNTs, there was increased thermomechanical and mechanical properties for 5.0 wt.% filler's ratio of the polyamide 12 (PA12)/MWCNT nanocomposite (5.0% wt.% incorporation of MWCNT into the PA12). By increasing filler's ratio up to the 10% wt.%, the electrical conductivity was increased. Growth of E. coli and S. aureus were inhibited as inhibition zone diameters of 2.1 and 2.5 mm, respectively by the 3D printed PA12/MWCNTs 10.0 wt.% nanocomposite specimen after 24 h incubation [58].

5. Conclusions

Biocompatible and biodegradable scaffold based on CNTs and fullerene can be prepared by 3D printing technology to improve attachment and migration of cells, delivering and retaining cells and biological macromolecules. Moreover, desirable reproducibility of experiments is the significant property for 3D printing technology. Results of docking study obtained from AutoDock Vina disclosed that CNTs compared to fullerenes had more affinity for bacterial virulence factors, which can be resulted from different morphology of CNTs (tubular shape) compared to fullerene (spherical shape). Totally, this study exhibited more affinity of CNT, capped CNT, C70, and C60 toward alpha-hemolysin (7AHL) of S. aureus compared to other virulence factors with values of -19.6, -18.8, -13.6, and -12.8 kcal/mol. Asparagine (ASN236 and ASN260: aliphatic amino acid) and serine (SER261: a polar amino acid) have found specifically for CNT-1MWT docking complex with the lowest binding energy of -20.1 kcal/mol. Additionally, the desirable conformational change and stability of CNT-1MWT complex at the different times have indicated according to the normal mode analysis of elNémo server and iMODS. For future studies, improving cellular uptake of CNTs and capped CNTs by surface functionalization such as ammonium and acetamide groups can be effective strategies. In the case of fullerenes, esterification (fullerene –COOR), carboxylation (fullerene–COOH), and hydroxylation (fullerene–OH) can be regarded to increase their hydrophilicity. In addition, loading some antibiotics such as sulfasalazine on the polyhydroxylated fullerene can be an effective strategy. The application of positive functional groups on CNTs surface such as lysine and arginine can improve antibacterial activity resulting from electrostatic adsorption of bacteria membrane with negative charge. Additionally, various antibiotics may apply to surface functionalize CNTs and

synergize their antibacterial activity against Gram-negative and Gram-positive bacteria. These carbon based nano-antibiotics has major industrialization potential with low toxicity, suitable for wound infections. Therefore, future in silico and in vitro studies should be focused on antibacterial activity of surface functionalized CNTs and fullerenes.

Author Contributions: Conceptualization, M.Al. and M.Ash.; methodology, M.Al.; software, M.Al.; validation, M.Al., M.Ash. and M.R.M.; formal analysis, M.Al.; resources, M.Ash.; data curation, M.Al.; writing—original draft preparation, M.Al.; review and editing, M.R.M.; visualization, M.Al.; supervision, M.Ash.. All authors have read and agreed to the published version of the manuscript.

Funding: This research received no external funding.

Institutional Review Board Statement: Not applicable.

Informed Consent Statement: Not applicable.

Conflicts of Interest: The authors declare no conflict of interest.

References

1. Amraei, S.; Eslami, G.; Taherpour, A.; Hashemi, A., Relationship between MOX genes and antibiotic resistance in Klebsiella pneumoniae strains in nosocomial infections. Micro Nano Bio Aspects 2022, 1, (2), 12-17.
2. Amraei, S.; Eslami, G.; Taherpour, A.; Hashemi, A., The role of ACT and FOX genes in Klebsiella pneumoniae strains isolated from hospitalized patients. Micro Nano Bio Aspects 2022, 1, (2), 18-25.
3. Amraei, S.; Ahmadi, S., Recent studies on antimicrobial and anticancer activities of saponins: a mini-review. Nano Micro Biosystems 2022, 1, (1), 22-26.
4. Alavi, M.; Jabari, E.; Jabbari, E., Functionalized carbon-based nanomaterials and quantum dots with antibacterial activity: a review. Expert Rev. Anti Infect. Ther. 2021, 19, (1), 35-44.
5. Riha, S. M.; Maarof, M.; Fauzi, M. B., Synergistic Effect of Biomaterial and Stem Cell for Skin Tissue Engineering in Cutaneous Wound Healing: A Concise Review. Polymers 2021, 13, (10), 1546.
6. Chung, J. J.; Im, H.; Kim, S. H.; Park, J. W.; Jung, Y., Toward Biomimetic Scaffolds for Tissue Engineering: 3D Printing Techniques in Regenerative Medicine. Frontiers in Bioengineering and Biotechnology 2020, 8.
7. Qu, M.; Wang, C.; Zhou, X.; Libanori, A.; Jiang, X.; Xu, W.; Zhu, S.; Chen, Q.; Sun, W.; Khademhosseini, A., Multi-Dimensional Printing for Bone Tissue Engineering. Advanced Healthcare Materials 2021, 10, (11), 2001986.
8. Shahrubudin, N.; Lee, T. C.; Ramlan, R., An Overview on 3D Printing Technology: Technological, Materials, and Applications. Procedia Manufacturing 2019, 35, 1286-1296.
9. Zhao, Y.-Q.; Yang, J.-H.; Ding, X.; Ding, X.; Duan, S.; Xu, F.-J., Polycaprolactone/polysaccharide functional composites for low-temperature fused deposition modelling. Bioactive Materials 2020, 5, (2), 185-191.
10. Wasserfall, F.; Hendrich, N.; Ahlers, D.; Zhang, J., Topology-aware routing of 3D-printed circuits. Additive Manufacturing 2020, 36, 101523.
11. Cui, M.; Pan, H.; Su, Y.; Fang, D.; Qiao, S.; Ding, P.; Pan, W., Opportunities and challenges of three-dimensional printing technology in pharmaceutical formulation development. Acta Pharmaceutica Sinica B 2021, 11, (8), 2488-2504.
12. Ardeshana, B.; Jani, U.; Patel, A., Influence of Bending Angle on Mechanical Performance of SWCNTs and DWCNTs Based on Molecular Mechanics: FE Approach. Journal of Vibration Engineering & Technologies 2022.
13. Nadeem, M. F.; Azeem, M.; Farman, I., Comparative study of topological indices for capped and uncapped carbon nanotubes. Polycyc. Aromatic Compounds 2022, 42, (7), 4666-4683.
14. Cui, H.; Yu, Y.; Li, X.; Sun, Z.; Ruan, J.; Wu, Z.; Qian, J.; Yin, J., Direct 3D printing of a tough hydrogel incorporated with carbon nanotubes for bone regeneration. Journal of Materials Chemistry B 2019, 7, (45), 7207-7217.
15. Li, L.; Qin, S.; Peng, J.; Chen, A.; Nie, Y.; Liu, T.; Song, K., Engineering gelatin-based alginate/carbon nanotubes blend bioink for direct 3D printing of vessel constructs. Int. J. Biol. Macromol. 2020, 145, 262-271.

16. Vidakis, N.; Petousis, M.; Kourinou, M.; Velidakis, E.; Mountakis, N.; Fischer-Griffiths, P. E.; Grammatikos, S.; Tzounis, L., Additive manufacturing of multifunctional polylactic acid (PLA)—multiwalled carbon nanotubes (MWCNTs) nanocomposites. Nanocomposites 2021, 7, (1), 184-199.
17. Kang, S.; Pinault, M.; Pfefferle, L. D.; Elimelech, M., Single-Walled Carbon Nanotubes Exhibit Strong Antimicrobial Activity. Langmuir 2007, 23, (17), 8670-8673.
18. Hou, W.; Shi, G.; Wu, S.; Mo, J.; Shen, L.; Zhang, X.; Zhu, Y., Application of Fullerenes as Photosensitizers for Antimicrobial Photodynamic Inactivation: A Review. Front. Microbiol. 2022, 13.
19. Ghanem, S. M.; Abd El-Baky, R. M.; Abourehab, M. A. S.; Fadl, G. F. M.; Gamil, N. G. F. M., Prevalence of Quorum Sensing and Virulence Factor Genes Among Pseudomonas aeruginosa Isolated from Patients Suffering from Different Infections and Their Association with Antimicrobial Resistance. Infection and drug resistance 2023, 16, 2371-2385.
20. Gupta, P.; Gupta, R. K.; Harjai, K., Multiple virulence factors regulated by quorum sensing may help in establishment and colonisation of urinary tract by Pseudomonas aeruginosa during experimental urinary tract infection. Indian J. Med. Microbiol. 2013, 31, (1), 29-33.
21. Seilie, E. S.; Bubeck Wardenburg, J., Staphylococcus aureus pore-forming toxins: The interface of pathogen and host complexity. Semin. Cell Dev. Biol. 2017, 72, 101-116.
22. Fishovitz, J.; Hermoso, J. A.; Chang, M.; Mobashery, S., Penicillin-binding protein 2a of methicillin-resistant Staphylococcus aureus. IUBMB life 2014, 66, (8), 572-577.
23. Malhotra, V.; Okon, B. P.; Satsangi, A. T.; Das, S.; Waturuocha, U. W.; Vashist, A.; Clark-Curtiss, J. E.; Saini, D. K., Mycobacterium tuberculosis PknK Substrate Profiling Reveals Essential Transcription Terminator Protein Rho and Two-Component Response Regulators PrrA and MtrA as Novel Targets for Phosphorylation. Microbiology Spectrum 2022, 10, (2), e01354-21.
24. Gijsbers, A.; Vinciauskaite, V.; Siroy, A.; Gao, Y.; Tria, G.; Mathew, A.; Sánchez-Puig, N.; López-Iglesias, C.; Peters, P. J.; Ravelli, R. B. G., Priming mycobacterial ESX-secreted protein B to form a channel-like structure. Current research in structural biology 2021, 3, 153-164.
25. Schuetz, A. N., Emerging agents of gastroenteritis: Aeromonas, Plesiomonas, and the diarrheagenic pathotypes of Escherichia coli. Semin. Diagn. Pathol. 2019, 36, (3), 187-192.
26. Johura, F.-T.; Parveen, R.; Islam, A.; Sadique, A.; Rahim, M. N.; Monira, S.; Khan, A. R.; Ahsan, S.; Ohnishi, M.; Watanabe, H.; Chakraborty, S.; George, C. M.; Cravioto, A.; Navarro, A.; Hasan, B.; Alam, M., Occurrence of Hybrid Escherichia coli Strains Carrying Shiga Toxin and Heat-Stable Toxin in Livestock of Bangladesh. Frontiers in Public Health 2017, 4.
27. Tian, W.; Chen, C.; Lei, X.; Zhao, J.; Liang, J., CASTp 3.0: computed atlas of surface topography of proteins. Nucleic Acids Res. 2018, 46, (W1), W363-W367.
28. Baek, K.; Shin, H.; Cho, M., Multiscale modeling of mechanical behaviors of Nano-SiC/epoxy nanocomposites with modified interphase model: Effect of nanoparticle clustering. Composites Sci. Technol. 2021, 203, 108572.
29. Trott, O.; Olson, A. J., AutoDock Vina: improving the speed and accuracy of docking with a new scoring function, efficient optimization, and multithreading. J. Comput. Chem. 2010, 31, (2), 455-461.
30. López-Blanco, J. R.; Aliaga, J. I.; Quintana-Ortí, E. S.; Chacón, P., iMODS: internal coordinates normal mode analysis server. Nucleic Acids Res. 2014, 42, (Web Server issue), W271-6.
31. Lopéz-Blanco, J. R.; Garzón, J. I.; Chacón, P., iMod: multipurpose normal mode analysis in internal coordinates. Bioinformatics 2011, 27, (20), 2843-50.
32. Kovacs, J. A.; Chacón, P.; Abagyan, R., Predictions of protein flexibility: first-order measures. Proteins 2004, 56, (4), 661-8.
33. Ghosh, P.; Bhakta, S.; Bhattacharya, M.; Sharma, A. R.; Sharma, G.; Lee, S.-S.; Chakraborty, C., A Novel Multi-Epitopic Peptide Vaccine Candidate Against Helicobacter pylori: In-Silico Identification, Design, Cloning and Validation Through Molecular Dynamics. Int. J. Pept. Res. Ther. 2021, 27, (2), 1149-1166.
34. Suhre, K.; Sanejouand, Y.-H., ElNémo: a normal mode web server for protein movement analysis and the generation of templates for molecular replacement. Nucleic Acids Res. 2004, 32, (suppl_2), W610-W614.
35. Bhattacharjee, M.; Banerjee, M.; Mukherjee, A., In silico designing of a novel polyvalent multi-subunit peptide vaccine leveraging cross-immunity against human visceral and cutaneous leishmaniasis: an immunoinformatics-based approach. J. Mol. Model. 2023, 29, (4), 99.
36. Bauer, J. A.; Pavlović, J.; Bauerová-Hlinková, V., Normal Mode Analysis as a Routine Part of a Structural Investigation. In Molecules, 2019; Vol. 24.

37. Al-Karmalawy, A. A.; Alnajjar, R.; Dahab, M.; Metwaly, A.; Eissa, I., Molecular docking and dynamics simulations reveal the potential of anti-HCV drugs to inhibit COVID-19 main protease. Pharmaceutical Sciences 2021, 27, (Covid-19), S109-S121.
38. Qin, S.; Xiao, W.; Zhou, C.; Pu, Q.; Deng, X.; Lan, L.; Liang, H.; Song, X.; Wu, M., Pseudomonas aeruginosa: pathogenesis, virulence factors, antibiotic resistance, interaction with host, technology advances and emerging therapeutics. Signal Transduction and Targeted Therapy 2022, 7, (1), 199.
39. Zeng, J.; Platig, J.; Cheng, T.-Y.; Ahmed, S.; Skaf, Y.; Potluri, L.-P.; Schwartz, D.; Steen, H.; Moody, D. B.; Husson, R. N., Protein kinases PknA and PknB independently and coordinately regulate essential Mycobacterium tuberculosis physiologies and antimicrobial susceptibility. PLoS Path. 2020, 16, (4), e1008452.
40. Zupetic, J.; Peñaloza, H. F.; Bain, W.; Hulver, M.; Mettus, R.; Jorth, P.; Doi, Y.; Bomberger, J.; Pilewski, J.; Nouraie, M.; Lee, J. S., Elastase Activity From Pseudomonas aeruginosa Respiratory Isolates and ICU Mortality. Chest 2021, 160, (5), 1624-1633.
41. Chadha, J.; Harjai, K.; Chhibber, S., Revisiting the virulence hallmarks of Pseudomonas aeruginosa: a chronicle through the perspective of quorum sensing. Environ. Microbiol. 2022, 24, (6), 2630-2656.
42. Bonifacius, A.; Goldmann, O.; Floess, S.; Holtfreter, S.; Robert, P. A.; Nordengrün, M.; Kruse, F.; Lochner, M.; Falk, C. S.; Schmitz, I.; Bröker, B. M.; Medina, E.; Huehn, J., Staphylococcus aureus Alpha-Toxin Limits Type 1 While Fostering Type 3 Immune Responses. Front. Immunol. 2020, 11.
43. Ramstad, S. N.; Wasteson, Y.; Lindstedt, B.-A.; Taxt, A. M.; Bjørnholt, J. V.; Brandal, L. T.; Bohlin, J., Characterization of Shiga Toxin 2a Encoding Bacteriophages Isolated From High-Virulent O145:H25 Shiga Toxin-Producing Escherichia coli. Front. Microbiol. 2021, 12.
44. Skariyachan, S.; Parveen, A.; Garka, S., Nanoparticle Fullerene (C60) demonstrated stable binding with antibacterial potential towards probable targets of drug resistant Salmonella typhi – a computational perspective and in vitro investigation. J. Biomol. Struct. Dyn. 2017, 35, (16), 3449-3468.
45. Ahmed, L.; Rasulev, B.; Turabekova, M.; Leszczynska, D.; Leszczynski, J., Receptor- and ligand-based study of fullerene analogues: comprehensive computational approach including quantum-chemical, QSAR and molecular docking simulations. Org. Biomol. Chem. 2013, 11, (35), 5798-5808.
46. Gopal, D.; Skariyachan, S.; Melappa, G., Chapter 8 - Molecular interaction modeling of carbon nanotubes and fullerene toward prioritized targets of SARS-CoV-2 by computer-aided screening and docking studies. In Functionalized Carbon Nanomaterials for Theranostic Applications, Mallakpour, S.; Hussain, C. M., Eds. Elsevier: 2023; pp 157-179.
47. Teixeira-Santos, R.; Gomes, M.; Gomes, L. C.; Mergulhão, F. J., Antimicrobial and anti-adhesive properties of carbon nanotube-based surfaces for medical applications: a systematic review. iScience 2021, 24, (1), 102001.
48. Zardini, H. Z.; Amiri, A.; Shanbedi, M.; Maghrebi, M.; Baniadam, M., Enhanced antibacterial activity of amino acids-functionalized multi walled carbon nanotubes by a simple method. Colloids Surf. B. Biointerfaces 2012, 92, 196-202.
49. Sharma, V. K.; McDonald, T. J.; Kim, H.; Garg, V. K., Magnetic graphene–carbon nanotube iron nanocomposites as adsorbents and antibacterial agents for water purification. Adv. Colloid Interface Sci. 2015, 225, 229-240.
50. Nie, C.; Yang, Y.; Cheng, C.; Ma, L.; Deng, J.; Wang, L.; Zhao, C., Bioinspired and biocompatible carbon nanotube-Ag nanohybrid coatings for robust antibacterial applications. Acta Biomater. 2017, 51, 479-494.
51. Hassani, M.; Tahghighi, A.; Rohani, M.; Hekmati, M.; Ahmadian, M.; Ahmadvand, H., Robust antibacterial activity of functionalized carbon nanotube- levofloxacine conjugate based on in vitro and in vivo studies. Sci. Rep. 2022, 12, (1), 10064.
52. Alavi, M.; Hamblin, M. R., Interaction of copper oxide nanoparticles with bacterial nucleic acids: a mini-review. Micro Nano Bio Aspects 2023, 2, (1), 20-25.
53. Aljelehawy, Q.; Maroufi, Y.; Javid, H.; Mohammadi, M. R.; Raji Mal Allah, O.; Taheri, S. V.; Mohammadzade, H., Anticancer, antineurodegenerative, antimicrobial, and antidiabetic activities of carvacrol: recent advances and limitations for effective formulations. Nano Micro Biosystems 2023, 2, (1), 1-10.
54. Kostarelos, K.; Lacerda, L.; Pastorin, G.; Wu, W.; Wieckowski, S.; Luangsivilay, J.; Godefroy, S.; Pantarotto, D.; Briand, J.-P.; Muller, S.; Prato, M.; Bianco, A., Cellular uptake of functionalized carbon nanotubes is independent of functional group and cell type. Nature Nanotechnology 2007, 2, (2), 108-113.

 doi:10.20944/preprints202306.0068.v1

55. Bai, Y.; Wu, X.; Ouyang, P.; Shi, M.; Li, Q.; Maimaiti, T.; Lan, S.; Yang, S.-T.; Chang, X.-L., Surface modification mediates the interaction between fullerene and lysozyme: Protein structure and antibacterial activity. Environmental Science: Nano 2021, 8, (1), 76-85.
56. Javed Ansari, M.; Soltani, A.; Ramezanitaghartapeh, M.; Singla, P.; Aghaei, M.; Khandan Fadafan, H.; Ardalan Khales, S.; Shariati, M.; Shirzad-Aski, H.; Balakheyli, H.; Sarim Imam, S.; Zafar, A., Improved antibacterial activity of sulfasalazine loaded fullerene derivative: computational and experimental studies. J. Mol. Liq. 2022, 348, 118083.
57. Angulo-Pineda, C.; Srirussamee, K.; Palma, P.; Fuenzalida, V. M.; Cartmell, S. H.; Palza, H., Electroactive 3D Printed Scaffolds Based on Percolated Composites of Polycaprolactone with Thermally Reduced Graphene Oxide for Antibacterial and Tissue Engineering Applications. Nanomaterials 2020, 10, (3), 428.
58. Vidakis, N.; Petousis, M.; Velidakis, E.; Tzounis, L.; Mountakis, N.; Boura, O.; Grammatikos, S. A., Multi-functional polyamide 12 (PA12)/ multiwall carbon nanotube 3D printed nanocomposites with enhanced mechanical and electrical properties. Adv. Compos. Mater 2022, 31, (6), 630-654.